 © The Authors. CC BY 4.0 Int. Licencee: SV-JME

Sediment Wear Characteristics of a Bulb-Type Tubular Turbine under Varying Sediment Concentrations and Cavitation Conditions

Xiaomei Guo[1,✉] – Yuhao Chen[1] – Zuchao Zhu[2] – Chen Jinlin[3] – Aminjon Gulakhmadov[4] – Saidabdullo Qurbonalizoda[5] – Vladimir Kukareko[6]

[1] Zhejiang University of Water Resource and Electric Power, Key Laboratory of Key Technologies for Mechanical Industry Hydroelectric Power Generation Pump Turbine, Zhejiang Key Laboratory of Pumps and Turbines, China
[2] Hefei General Machinery Research Institute Co., Ltd. China
[3] HangZhou JiangHe Hydro-Electric Science & Technology Co., Ltd. China
[4] Institute of Water Resources, Hydropower and Ecology of the National Academy of Sciences of Tajikistan, Tajikistan
[5] National Academy of Sciences of Tajikistan Center of Innovative Development of Science and New Technologies, Tajikistan
[6] Joint Institute of Mechanical Engineering, National Academy of Sciences of Belarus, Belarus

✉ gxm@zuwe.edu.cn

Abstract *To investigate the wear characteristics of bulb-type tubular turbine under sediment-laden cavitation conditions, this study examines the wear mechanisms of this turbine under the combined effect of particles and cavitation. Numerical simulations of sediment erosion were conducted for the turbine under different particle concentrations, based on the Euler–Lagrange approach and the Tabakoff wear model, considering both solid–liquid two-phase flows and solid–liquid–vapor three-phase flows. Comparison of sediment erosion under cavitating and non-cavitating conditions reveals that, under sediment-laden solid–liquid two-phase flow conditions, an increase in particle concentration increases wear. The wear rates of the draft tube, runner chamber, guide vanes, and runner increase with particle concentration. In contrast, the wear in Region 1 on the strut initially decreases and then increases as particle concentration increases. Additionally, the pressure on the bulb and guide vanes, as well as the turbulent kinetic energy in the draft tube, increase with particle concentration. Under sediment-laden solid–liquid–vapor three-phase flow conditions, wear varies considerably among turbine components. Particle concentration shows a positive correlation with the wear of the draft tube, runner chamber, and guide vanes. Notably, within the runner chamber, the runner experiences the most severe wear at a particle concentration of 4.5 %. Cavitation increases the pressure on the guide vanes and bulb wall surfaces, while it suppresses the turbulent kinetic energy in the draft tube and mitigates wall erosion.*

Keywords *solid–liquid–vapor three-phase flow, sediment-laden cavitation, bulb-type tubular turbine, solid–liquid two-phase flow, wear characteristics*

Highlights

- *This study employs numerical simulation to investigate the sediment wear behavior of bulb-type tubular turbines under cavitation conditions.*
- *The effects of particle concentration on wear, pressure and turbulence were investigated.*
- *Cavitation suppresses draft-tube wear but intensifies local runner-chamber wear.*
- *Concentration-dependent erosion mechanisms were identified.*

1 INTRODUCTION

The global transition to low-carbon energy is accelerating, and renewable energy has become an important priority worldwide. As a stable low-carbon renewable power source, hydropower has been widely developed. With a compact structure and good adaptability to low-head and high-flow conditions, bulb-type tubular turbines have been widely adopted in low-head hydropower plants worldwide [1] leading to improved operational performance and shorter equipment service life. Nevertheless, many sediment-laden river basins across the globe face severe erosion caused by the synergistic effects of cavitation and sediment particles, which damages turbine components [2]. Therefore, it is essential to investigate the sediment wear characteristics of bulb-type tubular turbines under varying sediment concentrations and cavitation conditions.

Extensive investigations have been conducted on the sediment wear mechanisms in hydraulic machinery, particle transport characteristics, and numerical prediction approaches for multiphase-flow erosion. Regarding sediment erosion patterns, Fan et al. [3] demonstrated through numerical simulations the asymmetric wear distribution of impulse turbine nozzles originates from particle-flow discrepancies. Xie et al. [4] analyzed the solid-liquid two-phase flow within runners and draft tubes, confirming that high sediment concentration and large-diameter particles exacerbate component wear. Kumar and Sarkar [5] combined numerical simulations with experiments to identify high-risk wear regions in Francis turbines. Song et al. [6] further demonstrated that guide-vane opening modulates particle trajectories inside Francis turbines, consequently altering the spatial pattern of sediment wear. Wei et al. [7] established correlations between the wear distribution of Francis runners and blade vortex structures as well as operating conditions. Regarding coupled cavitation–sediment erosion, numerous researchers have explored the interaction mechanisms through numerical simulations and experimental measurements. Lin et al. [8,9] performed numerical and experimental studies on sediment-laden cavitation in axial-flow pumps. They illustrated that sediment concentration modifies bubble distribution features and uncovered the coupling effect between cavitation and sediment wear. Han et al. [10] incorporated

 DOI: 10.5545/sv-jme.2026.1830

cavitation effects into wear computations for impulse-turbine buckets and analyzed the influencing role of cavitation on particle motion. Kevorkijan et al. [11] further numerically predicted particle erosion in a cavitating Pelton runner using Lagrangian tracking combined with the Finnie model, revealing a strong dependence of wear distribution on sediment concentration. Peng et al. [12] verified that microparticles enhance both cavitation intensity and material-removal capability of submerged cavitating jets. Experimental results from Chen et al. [13] indicated that sediment particle size and concentration markedly influence the cavitation-wear magnitude of sediment-laden flows. Wang et al. [14] carried out experiments under high-speed flow conditions to investigate the synergistic mechanism between cavitation erosion and particle wear. Beyond particle-related factors, Liu et al. [15] found through CFD that oil temperature and return pressure appreciably alter cavitation inception and bubble-collapse oscillations. Meanwhile, several studies have interpreted bubble-particle interaction dynamics at the microscale. Mitra et al. [16] visualized the interaction process between bubbles and particles in flotation devices. Wu et al. [17] investigated the motion behavior of near-wall spherical particles driven by laser-induced cavitation bubbles. Dai et al. [18] and Zhang et al. [19] investigated the respective effects of particle-bubble distance and particle-size ratio on bubble-collapse characteristics. Liu et al. [20] analyzed how fluid viscosity governs the development of jets induced by near-wall bubble collapse. Complementing these microscale studies, Vovk and Ravnik [21] compared 1D Euler and 3D Navier–Stokes models for water-hammer cavitation, confirming the capability of 3D volume-of-fluid methods to resolve bubble growth and collapse.

Previous studies demonstrate that considerable research has been conducted on sediment-laden solid–liquid wear and sediment-laden solid–liquid–vapor erosion in hydraulic turbines. However, the wear mechanisms of bulb-type tubular turbines under complex sediment-laden cavitation conditions remain unclear. Across a range of particle concentrations, this paper investigates sediment-induced erosion in bulb-type tubular turbines under cavitating and non-cavitating conditions.

2 MATHEMATICAL MODEL

Within the Euler–Lagrange framework, the shear-stress-transport (SST) k–ω turbulence model is used in this study to resolve the liquid-phase continuous flow field. The ZGB cavitation model is incorporated to describe the phase-change mass transfer between liquid and vapor phases. Two-way coupling is implemented between the continuous phase (liquid–vapor mixture) and discrete sand particles. The Tabakoff–Grant erosion model is employed to calculate sediment erosion on flow-passage surfaces.

2.1 Continuous-Phase Governing Equations

In the present study, the liquid phase is treated as a continuum and its governing equations are solved within a Eulerian framework. For an incompressible, viscous fluid, the continuity equation and the Reynolds-averaged momentum equation are expressed as follows:

$$\frac{\partial \rho}{\partial t} + \nabla \cdot (\rho \mathbf{u}) = 0, \tag{1}$$

$$\frac{\partial (\rho \mathbf{u})}{\partial t} + \nabla \cdot (\rho \mathbf{u}\mathbf{u}) = -\nabla p + \nabla \cdot \left[\mu \left(\nabla \mathbf{u} + \nabla \mathbf{u}^T \right) \right] + \mathbf{F}_s. \tag{2}$$

In Equations (1) and (2) ρ is the fluid density, $\mathbf{u}$ is the fluid velocity vector, p is the static pressure, μ is the dynamic viscosity, and $\mathbf{F}_s$ is the momentum-exchange source term exerted by the discrete-phase particles on the continuous phase (that is, the two-way coupling term), which is obtained by volume-averaging the reaction forces corresponding to the various fluid forces acting on the particles in the particle motion equations.

Under the solid–liquid–vapor three-phase flow (cavitating flow field) condition, the liquid and vapor phases constitute a homogeneous mixture; accordingly, the mixture density ρ_m and mixture viscosity μ_m are used to replace ρ and μ in the above equations.

$$\rho_m = \alpha_l \rho_l + \alpha_v \rho_v, \tag{3}$$

$$\mu_m = \alpha_l \mu_l + \alpha_v \mu_v. \tag{4}$$

In Equations (3) and (4) α_l and α_v denote the volume fractions of the liquid and vapor phases, respectively; ρ_l and ρ_v denote the corresponding densities of the liquid and vapor phases; and μ_l and μ_v denote the corresponding dynamic viscosities of the liquid and vapor phases. The transport of the vapor volume fraction is solved using the ZGB cavitation model.

2.2 Eulerian–Lagrangian Particle Tracking Model

In the present study, a Eulerian–Lagrangian approach is employed to numerically simulate the solid–liquid two-phase flow in a hydraulic turbine. The liquid phase is treated as a continuum, and the Navier–Stokes equations are solved within a Eulerian framework; sediment particles are treated as the discrete phase and tracked in a Lagrangian frame, with the trajectory, velocity, and position of each particle obtained by integrating the particle equations of motion.

The discrete-phase particles are subjected to various fluid forces in the flow field, and their motion is governed by Newton's second law. The equations for particle position and momentum are given as follows:

$$\frac{dx_p}{dt} = u_p, \tag{5}$$

$$m_p \frac{du_p}{dt} = F_D + F_{VM} + F_P + F_{Other}, \tag{6}$$

$$F_D = \frac{1}{2} C_D \rho_l A_p \left| u_f - u_p \right| \left(u_f - u_p \right). \tag{7}$$

In Equations (5) to (7) x_p is the particle position; t is time; u_p is the particle velocity; m_p is the particle mass; F_D is the drag force; F_{VM} is the virtual-mass force; F_P is the pressure-gradient force; F_{Other} represents other particle-interaction forces; C_D is the drag coefficient; ρ_l is the liquid density; A_p is the particle projected area; u_f is the local continuous-phase velocity.

In the internal flow of a hydraulic turbine, the drag force acting on the particles is much greater than gravity and other body forces; accordingly, gravity and secondary forces such as the Basset force and Saffman lift force are neglected in the present study. The virtual mass force and pressure gradient force are expressed as follows:

$$F_{VM} = \frac{1}{2} m_f \left(\frac{du_f}{dt} - \frac{du_p}{dt} \right), \tag{8}$$

$$F_P = m_f \frac{du_f}{dt}. \tag{9}$$

In Equations (8) and (9) m_f is the mass of fluid displaced by the particle.

2.3 Turbulence Model

The SST k–ω turbulence model consists of the transport equations for turbulent kinetic energy k and specific dissipation rate ω. A blending function F_1 is used to provide a smooth transition between the near-wall k–ω model and the far-field k–ε model.

Transport equation for turbulent kinetic energy k:

$$\frac{\partial(\rho k)}{\partial t}+\nabla\cdot(\rho \mathbf{U}k)=$$
$$=\nabla\cdot\left[(\mu+\sigma_k\mu_t)\nabla k\right]+P_k-\beta^*\rho\omega k. \quad (10)$$

Transport equation for specific dissipation rate ω:

$$\frac{\partial(\rho\omega)}{\partial t}+\nabla\cdot(\rho \mathbf{U}\omega)=\nabla\cdot\left[(\mu+\sigma_\omega\mu_t)\nabla\omega\right]$$
$$+\alpha\frac{\omega}{k}P_k-\beta\rho\omega^2+2(1-F_1)\rho\sigma_{\omega 2}\frac{1}{\omega}\nabla k\cdot\nabla\omega. \quad (11)$$

In Equations (10) and (11) ρ denotes density; $\mathbf{U}$ denotes the velocity vector; μ denotes molecular viscosity; P_k denotes the production term of turbulent kinetic energy; μ_t denotes turbulent viscosity, which is defined as follows:

$$\mu_t=\frac{\rho k}{\omega}\cdot\frac{a_1}{\max(a_1,\Omega F_2)}. \quad (12)$$

In Equation (12), $\Omega=\sqrt{2\Omega_{ij}\Omega_{ij}}$ represents the magnitude of vorticity, and Ω_{ij} denotes the rotation tensor.

$$F_1=\tanh\left(\left\{\min\left[\max\left(\frac{\sqrt{k}}{\beta^*\omega y},\frac{500\nu}{y^2\omega}\right),\frac{4\rho\sigma_{\omega 2}k}{CD_{k\omega}y^2}\right]\right\}^4\right), \quad (13)$$

$$F_2=\tanh\left(\left[\max\left(\frac{2\sqrt{k}}{\beta^*\omega y},\frac{500\nu}{y^2\omega}\right)\right]^2\right). \quad (14)$$

In Equations (13) and (14), y is the distance to the nearest wall, and $\nu=\mu/\rho$ is the kinematic viscosity. $CD_{k\omega}$ denotes the cross-diffusion term, whose expression is given below:

$$CD_{k\omega}=\max\left(2\rho\sigma_{\omega 2}\frac{1}{\omega}\nabla k\cdot\nabla\omega,10^{-10}\right). \quad (15)$$

The constants for the SST $k-\omega$ turbulence model are listed below:

$$\begin{cases}\beta^*=0.09, & a_1=0.31\\ \sigma_{k1}=0.85, & \sigma_{\omega 1}=0.5\\ \sigma_{k2}=1.0, & \sigma_{\omega 2}=0.856\\ \beta_1=0.075, & \beta_2=0.0828\\ \alpha_1=5/9, & \alpha_2=0.44\end{cases}. \quad (16)$$

2.4 ZGB Cavitation Model

The Zwart-Gerber-Belamri (ZGB) cavitation model is used in this study to simulate liquid-vapor phase change. Based on the homogeneous-flow assumption, this model solves the evolution of volume fraction via two-phase continuity equations. Piecewise mass source terms are used to describe bubble evaporation and growth, and condensation and collapse, separately, making the model suitable for simulating cavitating flows in hydraulic machinery. The continuity equations for liquid and vapor phases are given as follows:

$$\frac{\partial(\alpha_l\rho_l)}{\partial t}+\nabla\cdot(\alpha_l\rho_l\vec{u})=\dot{m}_{vl}, \quad (17)$$

$$\frac{\partial(\alpha_v\rho_v)}{\partial t}+\nabla\cdot(\alpha_v\rho_v\vec{u})=-\dot{m}_{vl}, \quad (18)$$

$$\alpha_l+\alpha_v=1. \quad (19)$$

In Equations (17) to (19) α_l and α_v represent the volume fractions of liquid and vapor phases, respectively; ρ_l and ρ_v denote the liquid-phase and vapor-phase densities; $\vec{u}$ is the mixture-phase velocity; $\dot{m}_{vl}$ stands for the mass-exchange source term between liquid and vapor phases.

The expressions for mass-transfer rates corresponding to bubble growth (evaporation) and collapse (condensation) are given as follows:

$$\dot{m}^+=F_{vap}\frac{3\alpha_{nuc}(1-\alpha_v)\rho_v}{R_B}\sqrt{\frac{2}{3}\frac{p_v-p}{\rho_l}}, \quad (20)$$

$$\dot{m}^-=F_{cond}\frac{3\alpha_v\rho_v}{R_B}\sqrt{\frac{2}{3}\frac{p-p_v}{\rho_l}}. \quad (21)$$

In Equations (20) and (21) $\dot{m}^+$ and $\dot{m}^-$ represent the mass-transfer rates for evaporation and condensation, respectively; F_{vap} and F_{cond} denote the evaporation coefficient and condensation coefficient; α_{nuc} is the volume fraction of initial cavitation nuclei; R_B stands for the bubble radius; p_v is the saturated vapor pressure of the fluid, and p is the local static pressure.

2.5 Tabakoff-Grant Model

The Tabakoff-Grant model is employed in this study to compute sediment wear on wall surfaces. Using particle impact velocity and impact angle as the principal parameters, the model quantifies material removal induced by particle impacts. Accordingly, all material damage referred to hereinafter in this paper originates from particle-induced erosion. This model accounts for the nonlinear effects of particle impact velocity and angle on the erosion rate. The model has been extensively validated in numerical simulations of sediment erosion for hydraulic machinery and is well-suited to the operating conditions investigated in the present work.

$$E=f(\gamma)\left(\frac{u_p}{u_1}\right)\cos^2\gamma\left(1-R_t^2\right)+\left(\frac{u_p}{u_2}\sin\gamma\right)^4, \quad (22)$$

$$f(\gamma)=\left[1+k_1k_{12}\sin\left(\frac{\pi\gamma}{2\gamma_0}\right)\right]^2, \quad (23)$$

$$R(t)=1-\frac{u_p}{u_3}\sin\gamma. \quad (24)$$

In Equations (22) to (24) E denotes the single-particle erosion ratio, with the unit of mg/g; γ is the particle impact angle; u_p is the particle impact velocity; u_1, u_2, and u_3 are reference velocity constants characterizing tangential cutting erosion, normal impact erosion and particle tangential rebound behavior, respectively; k_1, k_{12} and γ_0 are empirical parameters for the angle correction function; $R(t)$ represents the tangential rebound restitution coefficient of particles. The model constants are taken from [22], and their specific values are listed in Table 1.

Table 1. Particle property parameters

Particle/ Wall Material	Parameters					
	k_1	k_{12}	u_1 [m/s]	u_2 [m/s]	u_3 [m/s]	γ_0 [deg]
Quartz–Steel	1.0	0.29	123.72	352.99	179.29	30

3 NUMERICAL MODEL

3.1 Computational Domain and Mesh

This study examines a bulb-type tubular turbine. Figure 1 shows a three-dimensional exploded view of the turbine and a cross-sectional view of the fluid domain on the Y–Z plane. The bulb-type tubular

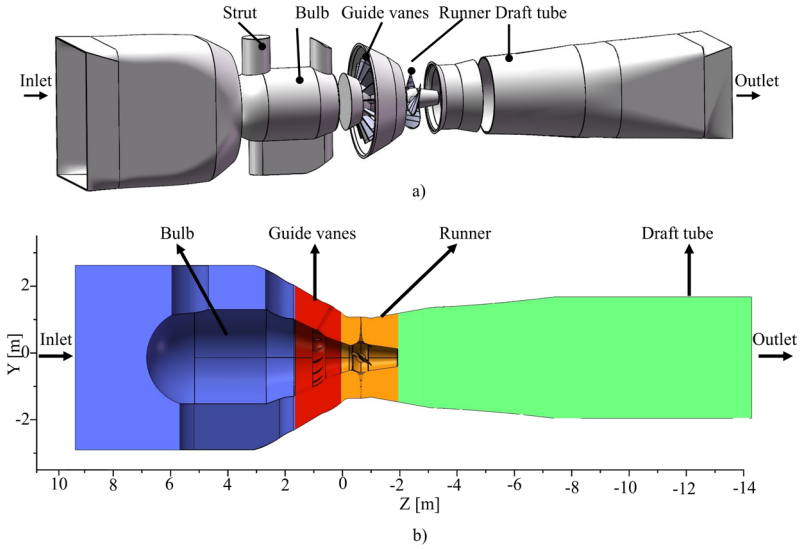


Fig. 1. a) Three-dimensional model of the bulb-type tubular turbine, and b) cross-section of computational domain of the bulb-type tubular turbine

turbine consists primarily of the strut, bulb, guide vanes, runner, and draft tube. This study investigates the sediment wear characteristics of a bulb-type tubular turbine under sand-laden cavitation conditions. The rated operating-condition parameters and main geometric dimensions of the bulb tubular turbine are summarized in Table 2. The rated operating parameters listed in Table 2 are derived from the comprehensive performance curve measured in the model test of the present study, and the efficiency values correspond to the rated operating point on that curve.

Table 2. Main geometric dimensions and performance parameters of the bulb tubular turbine

Rated parameters	Numerical values	Rated parameters	Numerical values
Head H	5.4 m	Flow rate Q	41.8 m^3/s
Efficiency η	94 %	Number of guide vanes Z_1	17
Rotational speed n	150 r/min	Number of runner blades Z_2	4
Runner diameter D	2.8 m	Total length	23.5 m

Figure 2 shows the mesh of the runner chamber and guide vanes of the bulb-type tubular turbine. To ensure mesh quality, mesh refinement was applied to the gap between the guide vanes and the runner. Because of the large size of the turbine under study, an unstructured mesh was adopted to reduce meshing complexity while maintaining mesh quality. All meshes used for the mesh-independence study have the same topology, and differences in mesh resolution are generated by adjusting the global size and boundary-layer nodes. The global mesh-size threshold is defined as the maximum element size. The wall y^+ value is maintained within the range of 20 to 50 to satisfy the calculation requirements of the turbulence model. Each mesh set differs in the total element count and the resolution of key regions, with a minimum element quality of 0.3. Figure 3 shows the efficiency–head curves of the bulb-type tubular turbine under different mesh resolutions. Turbine efficiency and head are selected as the output variables for mesh independence verification, and the relative variation is adopted as the error metric. As shown in Figure 3, when the mesh contains 1×10^7, the efficiency curve of the turbine stabilizes, with variations in the head curve not exceeding 1 %. To reduce the computational cost for subsequent simulations, a mesh consisting of 1×10^7 elements was selected for the numerical calculations.

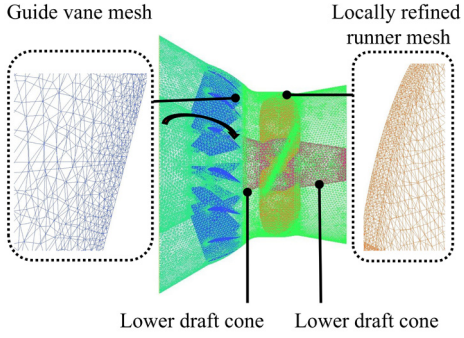


Fig. 2. Mesh of the bulb-type tubular turbine

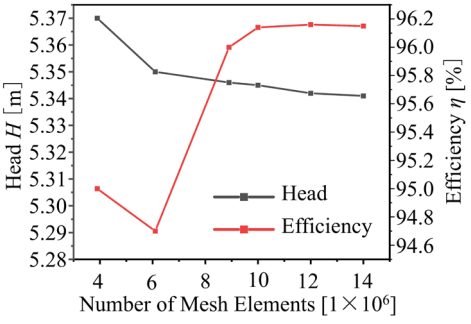


Fig. 3. Grid independence verification

3.2 Particle-independence verification

Particle-independence verification was performed to minimize computational error introduced by the parcel number of particles. Five particle-parcel counts of were selected for calculation: 5000, 7500, 10000, 12500, and 15000. As indicated by the average erosion rates in Table 3, when the particle parcel number reaches 12500, the wall-surface erosion rate and erosion distribution are consistent with those obtained for 15000 cases. Further increasing the particle parcel number has little effect on the simulation results. Considering

both computational accuracy and computational cost, a particle parcel number of 12500 was selected for the subsequent numerical calculations.

Table 3. Average erosion rate on the runner chamber wall under different computational particle parcel numbers

Case No.	Case 1	Case 2	Case 3	Case 4	Case 5
Particle parcel number	5,000	7,500	10,000	12,500	15,000
Erosion rate [kg/(m^{2}s)]	5.08×10^{-6}	4.79×10^{-6}	4.75×10^{-6}	4.6×10^{-6}	4.6×10^{-6}

3.3 Numerical Schemes and Boundary Conditions

Numerical simulations of the bulb-type tubular turbine were conducted using the Euler–Lagrange approach. The inlet was defined as a pressure boundary with a pressure of 45 kPa, and the outlet was set as a flow outlet with a flow rate of 41.8 m³/s. The solid-phase density was 2650 kg/m³. During the numerical simulation, the drag force is much greater than the gravitational force acting on the particles. Accordingly, the effect of gravity on the particles was neglected in the present study. Particle concentrations ranging from 1.5 % to 5.5 % were used, with a particle diameter of 0.75 mm and an inlet particle velocity of 1.16 m/s. Particle-particle collisions are neglected.

The runner domain was set as a rotating reference frame, and a frozen-rotor interface was defined between the rotating and stationary domains, with a rated rotational speed of 150 rpm. For steady-state calculations, the convergence criteria were defined as follows: the residuals of all continuous-phase variables were required to fall below 10^{-5}, and the monitored difference between inlet and outlet flow rates remained within 0.5 %. The flow field was considered converged when these conditions were met. The computational time required for full iterative convergence of a single operating case was approximately 8 hours.

Under the above-mentioned conditions, the sediment-cavitation erosion and the coupling effect discussed in this paper refer to changes in the flow-field environment that alter particle-induced erosion under sediment-laden cavitating conditions.

3.4 Experimental Validation

Figure 4a shows a photograph of the bulb of the bulb-type tubular turbine, and Fig. 4b shows a photograph of the guide vanes. Figure 5 presents a schematic diagram of the experimental setup for the bulb-type tubular turbine, which includes a particle injection system.

In the experimental setup of the bulb-type tubular turbine shown in Fig. 5, water flows from Tank 2, is pressurized by a pump, and then enters Tank 1 before being delivered to the inlet of the model turbine through the piping system. A pressure gauge is installed between Tank 1 and the model turbine. Above the system, a graduated particle hopper is positioned, and the particle content in the flow passage is controlled by a valve beneath the hopper, allowing particles to enter the model turbine simultaneously with the fluid. After passing through the model turbine, particles and fluid are separated in a settling tank, with the particles ultimately being collected in a storage container for subsequent recovery and reuse. The fluid returns from the settling tank to Tank 2, thereby maintaining circulation throughout the piping system.

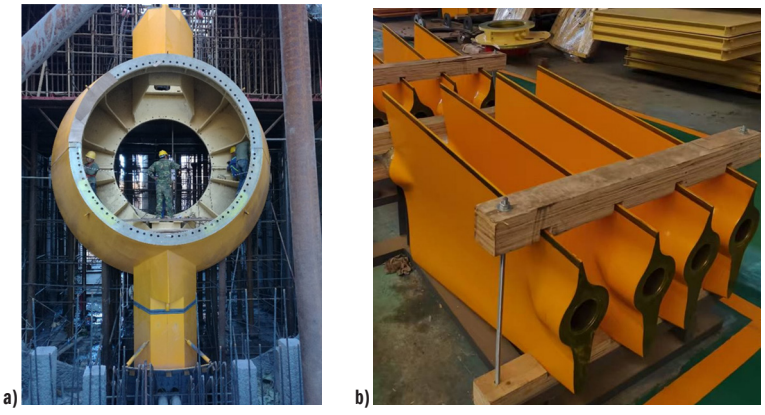


Fig. 4. Photographs of selected components; a) the bulb-type tubular turbine, and b) the guide vanes

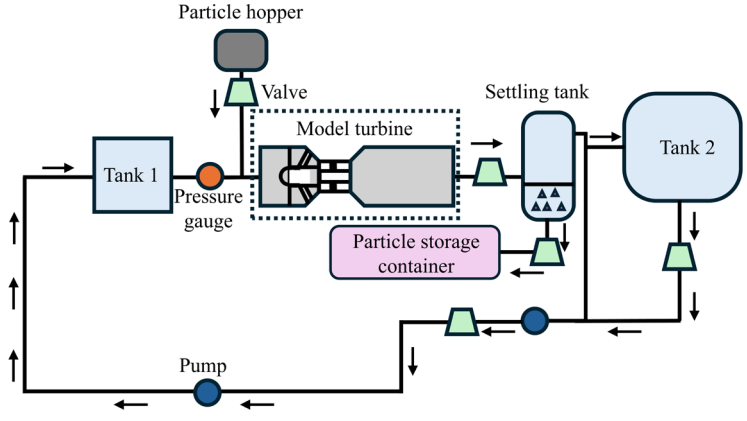


Fig. 5. Schematic of the experimental setup for the bulb-type tubular turbine

To verify the reliability of the numerical simulation, the simulated efficiency curve was compared with the experimentally measured efficiency curve. As shown in Figure 6, as the unit rotational speed increases, both the numerically calculated efficiency curve and the experimentally measured efficiency curve follow similar trends. The maximum error in efficiency occurs at a unit rotational speed of 205, reaching 3.2 %. The efficiency obtained from the numerical calculation is higher than that measured in the experiment because factors such as friction inside the turbine during the experiment lead to a slightly lower efficiency than that predicted by the numerical calculation. These results demonstrate that the numerical and experimental results follow similar trends, supporting the use of the numerical model in subsequent analyses.

Owing to experimental conditions, only the unit efficiency data are available for model validation in the present work, and no other measured parameters can be obtained. For sediment-erosion results, the analysis focuses on relative erosion distributions and trends rather than absolute erosion values. Therefore, the erosion prediction in this study carries inherent uncertainty, and the model cannot be fully validated in terms of erosion magnitude.

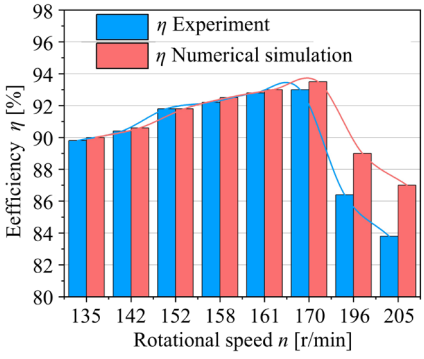


Fig. 6. Comparison of numerical and experimental efficiency characteristics

4 RESULTS AND DISCUSSION

To investigate the effects of particle concentration on the sediment wear characteristics of the bulb-type tubular turbine under sand-laden cavitation conditions, this study analyses the wall wear characteristics, cavitation behavior, and velocity characteristics of the turbine under different particle concentrations.

Figure 7 presents the wall wear rate curves and bar charts of the draft tube under different particle concentrations. The following can be observed: (1) regardless of the occurrence of cavitation, the wall wear rate of the draft tube exhibits an increase with particle concentration. At a particle concentration of 5.5 %, the wall wear rate of the draft tube reaches its maximum value of 2.93×10^{-8} kg/(m^{2}s). This is because, regardless of whether cavitation occurs, as particle concentration increases, the particle flux impacting the wall per unit time also increases, leading to a gradual increase in the wall wear rate of the draft tube. (2) The occurrence of cavitation suppresses the wear rate under the combined effect. At a particle concentration of 1.5 %, the difference in wall wear rate of the draft tube between the non-cavitating and cavitating conditions is 0.15×10^{-8} kg/(m^{2}s). Under the coupled cavitation-sediment effect, the particle-induced suppression of cavitation temporarily dominates at a particle concentration of 3.5 %, which produces a local minimum in the erosion rate. Subsequently, the erosion rate increases again as particle impingement becomes intensified. As particle concentration increases, the inhibitory effect of cavitation on wall wear gradually strengthens. When the particle concentration reaches 5.5 %, the wall wear rate of the draft tube decreases by 0.86×10^{-8} kg/(m^{2}s). This phenomenon has also been reported in [19]. The reasons for this phenomenon are twofold: (1) Cavitating flow modifies the flow-field conditions and further affects the particle motion trajectories. The originally directed and concentrated particle flow becomes more dispersed, causing the wear pattern to transition from continuous sheet-like erosion to more uniform wear. Furthermore, particles no longer cluster to impact the wall, reducing both the frequency and intensity of particle impacts on the draft tube wall; (2) The occurrence of cavitation alters the flow characteristics inside the draft tube, exerts a retarding effect on particle motion and reduces particle kinetic energy, which further influences the severity of sediment erosion.

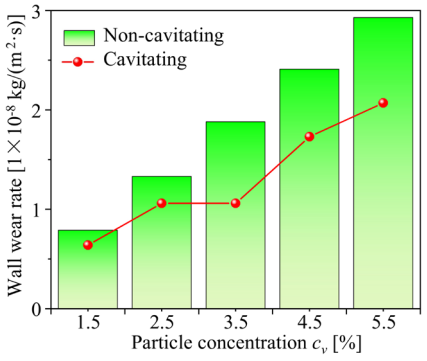


Fig. 7. Wall wear rate curves of the draft tube under different particle concentrations

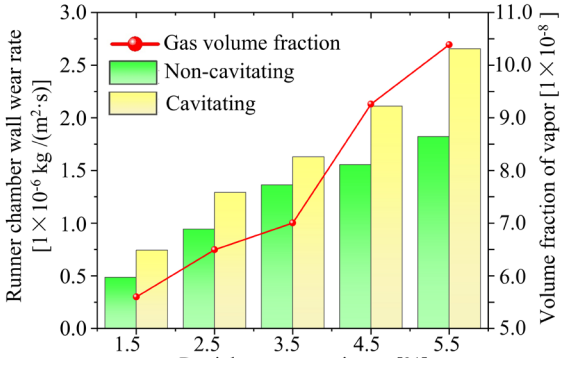


Fig. 8. Wear rate and cavitation bubble volume fraction in the runner chamber under different particle concentrations

Figures 8 and 9 show the wall wear rate and cavitation bubble volume fraction curves, respectively, along with the spatial distributions of bubbles in the runner chamber under different particle concentrations. The following trends can be observed: (1) as particle concentration increases, regardless of whether cavitation occurs, the wall wear rate of the runner chamber and the bubble volume fraction are positively correlated with particle concentration. The bubble volume fraction reaches its maximum value, of 9.8×10^{-8}, at a particle concentration of 5.5 %, indicating that increasing particle concentration enhances the degree of cavitation. This is because discrete-phase particles inversely modulate the characteristics of the continuous-phase flow field under the two-way coupling mechanism. As the particle concentration increases, particle–fluid interactions become stronger, which further modifies the local pressure distribution and promotes the generation and expansion of low-pressure regions, thereby intensifying cavitation. (2) Cavitation intensifies wall erosion in the runner chamber, and the bubbles primarily appear at the outer edges and hub of the runner blades. This is because cavitation bubbles occupy the part of flow-passage space when cavitation occurs, compressing the effective flow cross-section

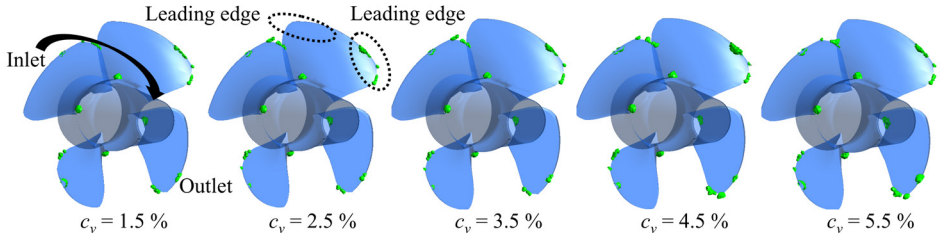


Fig. 9. Cavitation bubble distributions under different particle concentrations (α_v = 0.1).

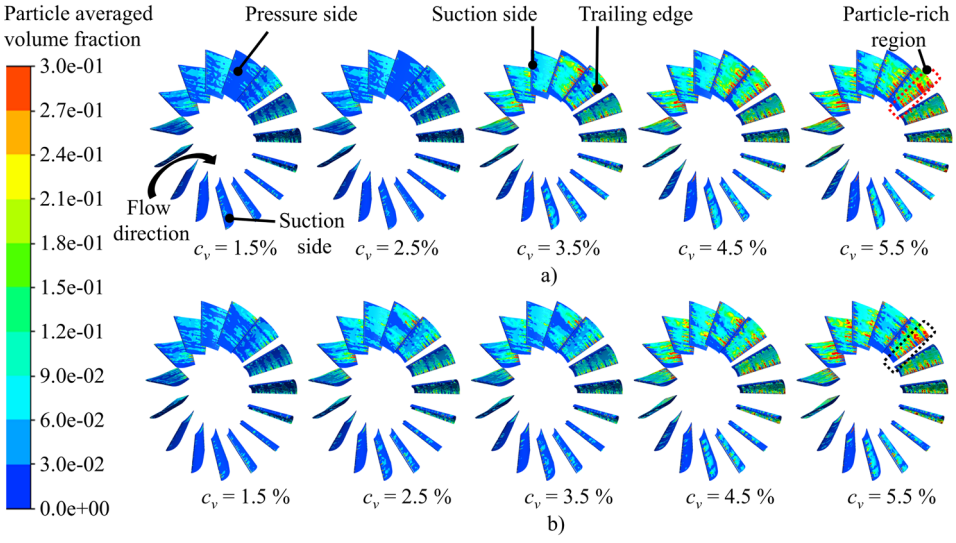


Fig. 10. Particle distribution on the guide vane walls under different particle concentrations; a) non-cavitating, and b) cavitating

and increasing the local flow velocity, which raises particle momentum and thus aggravates the erosion on the runner-chamber wall. As the particle concentration increases, the coupling and momentum exchange between particles and cavitation bubbles are further strengthened, amplifying this erosion effect.

Figure 10 shows the distribution of particle volume fraction on the guide-vane wall under different particle concentrations. The overall particle volume fraction on the guide-vane wall increases with rising particle concentration. Pronounced particle accumulation appears at the vane leading edge when the particle concentration reaches 5.5 %. Cavitation significantly modifies local particle distribution. At particle concentrations of 1.5 % to 2.5 %, cavitation aggravates particle accumulation on the wall and increases the particle volume fraction on the guide-vane surface. By contrast, the degree of particle aggregation at high concentrations on the guide-vane wall weakens at 5.5 % particle concentration.

Driven by inertia, particles do not readily follow changes in flow direction when passing through guide vanes. They tend to impact the vane leading edge and accumulate there. For low-concentration cases, the particle loading is low and the reverse modulation of particles on

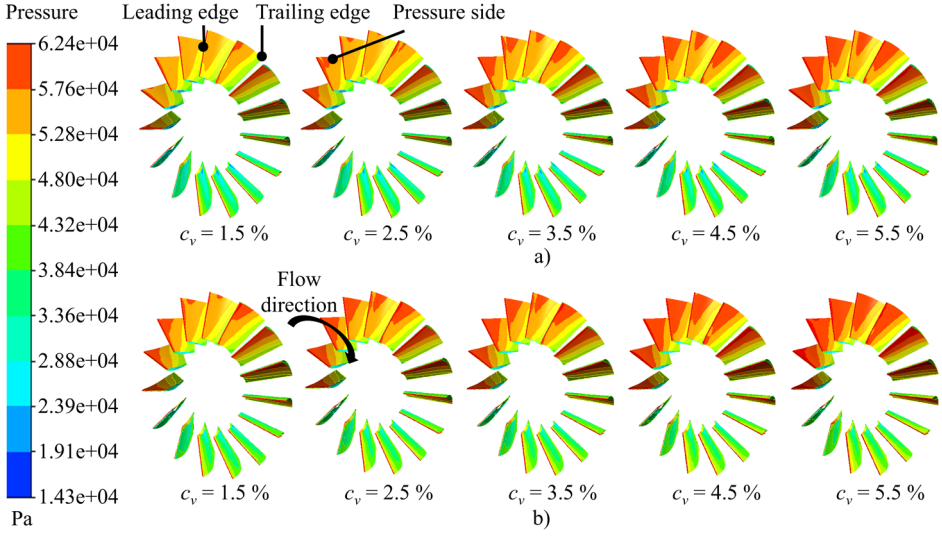


Fig. 11. Pressure distribution on the guide vane walls under different particle concentrations; a) non-cavitating, and b) cavitating

the liquid-phase flow field is negligible; the pressure and velocity fluctuations induced by cavitation therefore dominate particle motion, pushing particles toward the wall and raising near-wall particle content. Under high-concentration conditions, the number of particles increases, and the particle–fluid two-way coupling is intensified. The effect of particles on the liquid-phase flow field gradually becomes dominant, while the regulating effect of cavitation on the flow field becomes relatively weaker, thereby reducing near-wall particle accumulation.

Figure 11 shows the pressure distribution on the guide vane walls under different particle concentrations. From the figure, the following observations can be made: (1) regardless of the presence of cavitation, the pressure near the leading edge is relatively high, and the overall pressure on the guide vanes increases as particle concentration increases; (2) the occurrence of cavitation further increases pressure on the guide-vane walls. This is because, as particles pass the leading edge, they tend to maintain their original trajectories due to inertia. With increasing particle concentration, the resistance and pressure exerted by the solid particles on the liquid phase increase, reducing the fluid velocity near the guide vane walls and, thereby, increasing the wall pressure. The formation of cavitation regions changes the local flow pattern around the guide vanes and leads to an overall rise in static pressure on the guide-vane walls, which is a consequence of the coupling effect among solid-liquid-vapor three-phase flows.

Figure 12 shows the average wear rate curves of the runner under different particle concentrations. The figure shows that (1) in the absence of cavitation; the average wall wear rate of the runner exhibits a positive correlation with particle concentration. This is because, without cavitation, an increase in particle concentration leads to a higher frequency of particle impacts on the runner, resulting in an increased wear rate. (2) At a particle concentration of 1.5 %, the introduction of cavitation increases the average wear rate of the runner; however, at particle concentrations between 2.5 % and 5.5 %, cavitation suppresses wall wear on the runner. The maximum difference in wear rate between cavitating and non-cavitating conditions occurs at a particle concentration of 3.5 %, reaching 1.201×10^{-6} kg/(m^{2}s). This is attributed to the large number of cavitation bubbles. Bubble collapse modifies the local flow-field structure and further alters the motion of sediment particles, increasing the momentum of particles impacting the runner wall. The particle-acceleration effect induced by flow-field variation dominates, thereby increasing erosion. As the particle concentration increases (2.5 % to 4.5 %), the degree of cavitation intensifies, causing enhanced near-wall particle slip. The particle trajectories shift from the original 'direct-impact' type to a 'glancing' type, reducing the impact angle. Consequently, cavitation suppresses runner wear at moderate particle concentrations (2.5 % to 4.5 %). It is worth noting that within the particle-concentration range of 2.5 % to 3.5 %, the effect of cavitation on the flow field counteracts the enhanced erosion induced by increasing particle concentration, thereby keeping the erosion rate stable. At a particle concentration of 5.5 %, the particle loading is excessively high, and the particle–fluid two-way coupling is significantly enhanced. The effective density and viscosity of the local flow field increase, which strengthens the fluid retardation effect on particle motion and reduces the momentum with which particles impinge on the runner wall; consequently, the wall wear rate decreases at a concentration of 5.5 %.

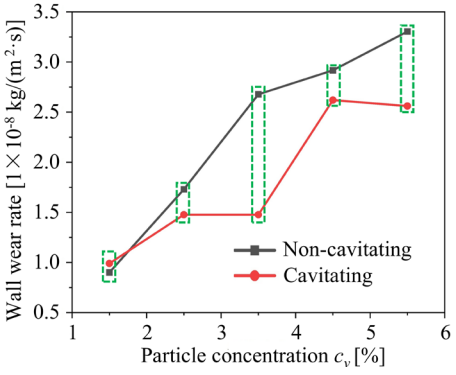


Fig. 12. Runner wear rate curves under different particle concentrations

Figure 13 shows the pressure distribution on the bulb under different particle concentrations. The figure shows the following: (1) the pressure on the bulb gradually decreases along the flow direction, exhibiting a clear pressure gradient. When the particle concentration increases from 1.5 % to 3.5 %, a localized high-pressure region appears at the top of the bulb. As the particle concentration further increases, the overall pressure rises, and the high-pressure region gradually extends downstream along the flow direction. This is because the increased particle concentration leads to higher local fluid density and viscosity, causing a local blockage at the top of the bulb, which reduces the fluid velocity and forms the high-pressure

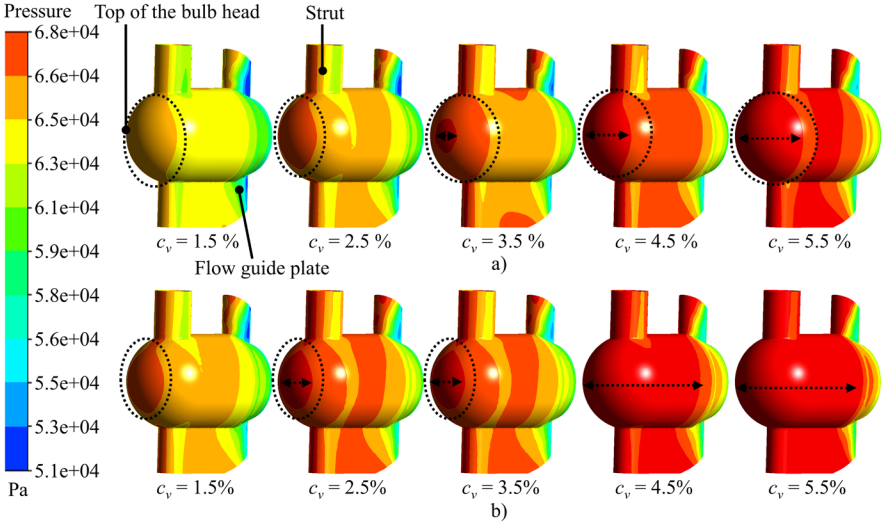


Fig. 13. Pressure distribution on the bulb under different particle concentrations; a) non-cavitating, and b) cavitating

region. Meanwhile, the increase in particle concentration intensifies the interactions and collisions between particles and the bulb head wall, resulting in an overall pressure increase on the bulb-head surface. (2) Cavitation leads to an overall increase in the pressure on the bulb, with pressure exhibiting a positive correlation with particle concentration. When the particle concentration reaches 5.5 %, the bulb exhibits a generally high-pressure state. This is because cavitation-bubble collapse disturbs the local flow-field distribution and induces variations in the pressure field, which further modifies the motion trajectories and forces acting on sediment particles. Two factors contribute to this pressure increase with particle concentration: first, increasing particle concentration enhances particle frictional resistance; second, bubble collapse reshapes the surrounding flow-field distribution and further changes the forces acting on sediment particles and their motion. As the particle concentration increases, the coupling effect between cavitating flow field and particles is continuously strengthened, and the flow-field pressure rises accordingly.

Figure 14 shows the wear distribution on the bulb head under different particle concentrations. From the figure, the following can be observed: (1) the wear on the strut initially decreases and then increases with increasing particle concentration. At a particle concentration of 5.5 %, the wear rate reaches its maximum value of 9.52×10^{-8} kg/(m^{2}s). This is because, at low to moderate concentrations (1.5 % to 4.5 %), the momentum exchange between particles and fluid is enhanced, and the viscosity of the wake increases. Some particles are entrained by the fluid, reducing the number of particles directly impacting the strut wall. The vortical regions are suppressed, and the number of particles stagnating in these regions decreases, resulting in reduced wall wear. When particle concentration increases to 5.5 %, the particle–fluid two-way coupling is intensified, and the local flow-field structure changes. The retention and accumulation of particles in the vortical region near the strut are enhanced, and the momentum of particles impinging on the strut wall increases, ultimately leading to aggravated wall wear. (2) Under the combined effects of sediment-laden cavitation, the wear in Region 1 exhibits a positive correlation with particle concentration, and the presence of cavitation further increases wear in this region, while no significant wear is observed in other areas. This is because the localised high-pressure regions generated during bubble collapse reduce the local mixture density and enhance the impact load. The combined effect of this with particle collisions leads to increased wall wear with increasing particle concentration. Additionally, in the vicinity of Region 1, the flow velocity and vortex intensity are high, resulting in large local shear forces, which cause particles to stagnate and impact near the strut; therefore, wear is concentrated primarily in Region 1. In this paper, contour plots for flow-field parameters such as vorticity distribution and shear stress are not presented separately. The above analyses regarding vortex and shear effects are summarized based on the observed evolution of the overall flow-field structure.

Figure 15 shows the two-dimensional distribution of turbulent kinetic energy in the draft tube under different particle concentrations. The position of the cross-section corresponds to that in Fig. 1b. From Figure 15a, the following can be observed: (1) the regions of high turbulent kinetic energy in the draft tube are mainly located in the central main flow and near the shear layers, exhibiting a clearly symmetrical distribution, with the maximum turbulent kinetic energy reaching 0.8 m^2/s^2; (2) regardless of the presence of cavitation, the turbulent kinetic energy intensity in the draft tube gradually increases with increasing particle concentration. This is because the strong swirling flow exiting the runner enters the draft tube, forming a high-velocity gradient between the central main flow and the peripheral low-speed regions, which destabilizes the shear layers, resulting in high-intensity turbulent kinetic energy regions near the central main flow and shear layers. As the particle concentration increases, momentum exchange between the particle inertia and the liquid phase is enhanced, causing particles to accumulate in the shear layers and low-speed recirculation regions, which amplifies local velocity fluctuations and expands the regions of high turbulent kinetic energy. It can be seen from Fig. 15b that the introduction of cavitation suppresses the magnitude of turbulent kinetic energy inside the draft tube. Several factors may explain this phenomenon. First, cavitation reduces the mean density of the flow field. According to the formula for turbulent kinetic energy:

$$k = \frac{1}{2}\overline{u_i' u_i'} \tag{25}$$

In Equation (25), k is the turbulent kinetic energy with the unit of m^2/s^2; u_i' denotes the fluctuating component of the fluid velocity with the unit of m/s. A reduction in the mixture density of the flow field leads to a significant decrease in the turbulent kinetic energy k. Second, the formation of cavitation vortices alters the pressure distribution in the flow field, suppresses the development of laminar

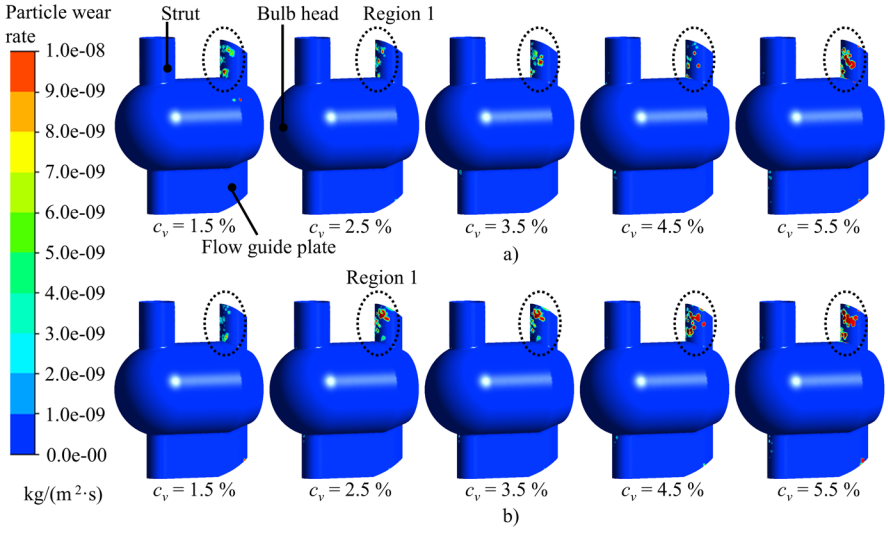


Fig. 14. Particle wear-rate distribution on the bulb head at different particle concentrations; a) non-cavitating, and b) cavitating

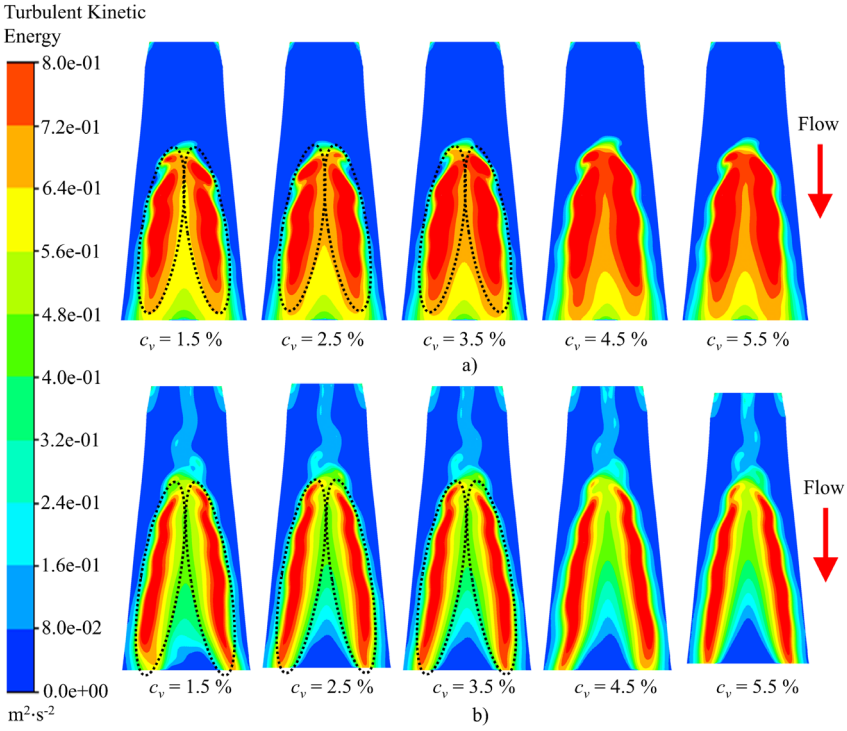


Fig. 15. Two-dimensional distribution of turbulent kinetic energy in the draft tube under different particle concentrations (Y-Z Plane); a) non-cavitating, and b) cavitating

and recirculating regions in the boundary layer, and reduces the local velocity gradients of the fluid, thereby inhibiting the intensity of turbulent kinetic energy.

5 CONCLUSIONS

In this paper, numerical simulations of particle erosion are carried out for a bulb-type tubular turbine under solid-liquid two-phase flow and solid-liquid-vapor three-phase flow (with cavitation) conditions, respectively. The study focused on the effects of particle concentration and cavitation on the wear characteristics of key flow components of the turbine, the cavitation characteristics near the runner, and the turbulent kinetic energy characteristics in the draft tube.

1. The influence of particle concentration on the wear characteristics of the bulb-type axial-flow turbine was revealed.
   Under solid–liquid two-phase flow conditions, as the particle concentration increases, the number of particles transported toward the walls grows and the two-way momentum exchange between particles and the liquid phase is strengthened; both effects jointly increase the frequency and intensity of particle impacts and shear on the walls. This results in a positive correlation between particle concentration and wear of the draft tube, runner chamber, guide vanes, and runner. In Region 1, wear initially decreases and then increases with increasing particle concentration.
2. The coupled erosion mechanism between cavitation and particles is clarified.
   The combined effect of cavitation and particles on erosion varies substantially among turbine components. Inside the runner chamber, cavitation and particle concentration promote each other. At low particle concentration (1.5 %), cavitation aggravates runner erosion, whereas cavitation suppresses runner erosion at moderate to high concentrations (2.5 % to 5.5 %). Cavitation consistently produces a suppressive effect on wall erosion in the draft tube.
3. The effects of particle concentration on wall wear and the flow field under complex solid–liquid–vapor three-phase flow conditions were revealed.
   Under solid–liquid–vapor three-phase flow conditions, the particle concentration exhibits a positive correlation with wear of the draft tube, runner chamber, and guide vanes. As the particle concentration increases, the runner wear first increases and then decreases, reaching a maximum at a particle concentration of 4.5 %. Particle concentration and cavitation are positively correlated with pressure on the guide vane walls; as particle concentration increases, pressure rises.
4. The effects of particle concentration and cavitation on flow-field characteristics were clarified.
   Particle concentration and cavitation exhibit a positive correlation with the pressure on the guide vane and bulb walls. An increase in particle concentration enhances turbulent kinetic energy in the draft tube, with a maximum turbulent kinetic energy of 0.8 m²/s². The occurrence of cavitation suppresses the turbulent kinetic energy in the draft tube and increases the wall pressure of guide vanes and the bulb head.

The findings of this paper clarify the erosion distribution characteristics and flow-field evolution law of bulb-type tubular turbines under complex multiphase flow conditions. This work addresses the limited previous research on the solid-liquid-vapor three-phase coupled erosion mechanism for bulb-tubular units in the literature. The conclusions provide a basis for structural optimization, the development of erosion-protection measures, and the development of safe and stable operating strategies for bulb-type tubular turbines operating in sediment-laden rivers.

References

[1] Li, Q., Zhou, F., Wang, Q. Flow Characteristics of Bulb Tubular Turbine Based on Solid-liquid Two-phase Flow Model. *J Appl Fluid Mech 18* 2137-2148 (2025) **DOI:10.47176/jafm.18.8.3320**.

[2] Shrestha, R., Pradhan, S.S., Gurung, P., Ghimire, A., Chitrakar, S. A review on erosion and erosion induced vibrations in Francis turbine. *IOP Conf Ser: Earth Environ Sci 1037* 012028 (2022) **DOI:10.1088/1755-1315/1037/1/012028**.

[3] Fan, W.R., Guo, P.C., Sun, L.G., Zheng, X.B. Numerical assessment of erosion wear in Pelton turbine injectors. *J Phys: Conf Ser 2707* 012067 (2024) **DOI:10.1088/1742-6596/2707/1/012067**.

[4] Xie, G., Li, Q., Xin, L., Li, Z. Analysis of solid-liquid two-phase flow in the area of rotor and tailpipe. *Processes 11* 3382 (2023) **DOI:10.3390/pr11123382**.

[5] Kumar, R., Sarkar, S. Erosion analysis of radial flow hydraulic turbine components through FLUENT-EDEM coupling. *Powder Technol 428* 118800 (2023) **DOI:10.1016/j.powtec.2023.118800**.

[6] Song, X., Zhou, X., Song, H., Deng, J., Wang, Z. Study on the effect of the guide vane opening on the band clearance sediment erosion in a Francis turbine. *J Marine Sci Eng 10* 1396 (2022) **DOI:10.3390/jmse10101396**.

[7] Wei, X.Y., Pei, J., Wang, W.Q., Yu, Z.F. Numerical study on sediment erosion characteristics of Francis turbine runner. *Eng Fail Analys 161* 108270 (2024) **DOI:10.1016/j.engfailanal.2024.108270**.

[8] Lin, P., Hu, D., Lu, J.M., Wang, S. CFD numerical simulation of sand-contained cavitation characteristics of axial-flow pump. *Adv Mech Eng 13* 16878140211032785 (2021) **DOI:10.1177/16878140211032785**.

[9] Lin, P., Hu, D., Lin, Z., Liu, M., Tang, C., Wang, S. The mechanism of joint effects of axial-flow pump cavitation and sediment wear. *Adv Mech Eng 12* 1687814020923066 (2020) **DOI:10.1177/1687814020923066**.

[10] Han, L., Guo, C., Yuan, Y., Li, D., Liu, Y., Iranzo, A. et al. Investigation on sediment erosion in bucket region of Pelton turbine considering cavitation. *Phys Fluid 36* (2024) **DOI:10.1063/5.0179387**.

[11] Kevorkijan, L., Hriberšek, M., Lešnik, L., Škerlavaj, A., Biluš, I. Numerical investigation of erosion due to particles in a cavitating flow in Pelton turbine. *Stroj vest-J Mech E 71* 284-293 (2025) **DOI:10.5545/sv-jme.2025.1351**.

[12] Peng, C., Tian, S., Li, G., Wei, M. Enhancement of cavitation intensity and erosion ability of submerged cavitation jet by adding micro-particles. *Ocean Eng 209* 107516 (2020) **DOI:10.1016/j.oceaneng.2020.107516**.

[13] Chen, S.Y., Xu, W.L., Luo, J., Li, J.B., Zhai, Y.W. Experimental study on the mesoscale causes of the effect of sediment size and concentration on material cavitation erosion in sandy water. *Wear 488* 204114 (2022) **DOI:10.1016/j.wear.2021.204114**.

[14] Wang, X., Hu, Y.A., Li, Z.H. Experimental study on the mechanism of the combined action of cavitation erosion and abrasion at high speed flow. *Int J Conc Struct Mater 13* 58 (2019) **DOI:10.1186/s40069-019-0374-8**.

[15] Liu, P., Zhao, Q., Peng, S., Quan, W., Gao, Z. The effects of oil temperature and oil return pressure on oil film damping characteristics of a high-speed solenoid valve. *Stroj vest-J Mech E 71* 83-91 (2025) **DOI:10.5545/sv-jme.2024.1168**.

[16] Mitra, S., Hoque, M.M., Evans, G., Nguyen, A.V. Direct visualisation of bubble-particle interactions in presence of cavitation bubbles in an ultrasonic flotation cell. *Mineral Eng 174* 107258 (2021) **DOI:10.1016/j.mineng.2021.107258**.

[17] Wu, S., Li, B., Zuo, Z., Liu, S. Dynamics of a single free-settling spherical particle driven by a laser-induced bubble near a rigid boundary. *Phys Rev Fluid 6* 093602 (2021) **DOI:10.1103/physrevfluids.6.093602**.

[18] Dai, Y., Zhang, H., Chen, T. Influence of bubble-particle distance on the dynamic behaviors of a cavitation bubble near a particle. *J Hydrodyn 35* 913-922 (2023) **DOI:10.1007/s42241-023-0063-6**.

[19] Zhang, H., Dai, Y., Yang, J.Q., Chen, T. Simulation of the effect of particle-bubble size ratio on the collapsing dynamics of a cavitation bubble near a particle. *J Phys Conf Ser 2752* 012193 (2024) **DOI:10.1088/1742-6596/2752/1/012193**.

[20] Liu, X., He, J., Lu, J., Ni, X. Effect of liquid viscosity on a liquid jet produced by the collapse of a laser-induced bubble near a rigid boundary. *Jap J Appl Phys 48* 016504 (2009) **DOI:10.1143/jjap.48.016504**.

[21] Vovk, N., Ravnik, J. Comparison of 1D Euler equation based and 3D Navier-Stokes simulation methods for water hammer phenomena. *Stroj vest-J Mech E 71* 337-348 (2025) **DOI:10.5545/sv-jme.2025.1340**.

[22] Tabakoff, W., Grant, G., Ball, J.R. An experimental investigation of certain aerodynamic effects on erosion. AIAA Paper 74-639 (1974) **DOI:10.2514/6.1974-639**.

Acknowledgements *This work was supported by National Key R&D Program Project (No. 2025YFE0102900), and The International Cooperation and Exchange Projects of the National Natural Science Foundation of China" (W2521089), and Key Research and Development Project of Hangzhou City (2024SZD1B17). Central Funds Guiding the Local Science and Technology Development Projects (2025ZY01030). Key Projects of the Ministry of Water Resources (KS-2025076).*

Received *2026-06-05,* **revised** *2026-08-26, 2026-09-29*
accepted *2026-10-09 as Original Scientific Paper.*

Data Availability *The data supporting the findings of this study are included in the article and/or its supplementary materials.*

Author Contribution *Xiaomei Guo: Supervision, Conceptualization, Funding acquisition, Methodology, Writing – review & editing. Yuhao Chen: Software, Validation, Formal analysis, Visualization, Writing – original draft. Zuchao Zhu: Methodology, Verification. Chen Jinlin: Resources, Data curation. Aminjon Gulakhmadov: Writing – review & editing. Saidabdullo Qurbonalizoda: Formal analysis, Writing – review & editing. Vladimir Kukareko: Supervision, Writing – review & editing. All authors reviewed and approved the final manuscript.*

AI Assisted Writing *No AI tools were used in the preparation of this manuscript. All content and conclusions remain the responsibility of the authors.*

Značilnosti erozijske obrabe zaradi sedimentnih delcev v cevni turbini pri različnih koncentracijah sedimenta in kavitacijskih pogojih

Povzetek *Za raziskavo značilnosti obrabe cevne turbine pri kavitacijskih pogojih ob prisotnosti sedimentnih delcev so bili analizirani mehanizmi obrabe turbine zaradi kombiniranega vpliva trdnih delcev in kavitacije. Numerične simulacije erozijske obrabe zaradi sedimentnih delcev so bile izvedene pri različnih koncentracijah delcev na podlagi Euler-Lagrangeevega pristopa in Tabakoffovega modela obrabe, pri čemer sta bila obravnavana dvofazni tok trdnih delcev in tekočine ter trifazni tok trdnih delcev, tekočine in pare. Primerjava erozijske obrabe pri pogojih s kavitacijo in brez nje je pokazala, da se pri dvofaznem toku trdnih delcev in tekočine obraba povečuje z naraščajočo koncentracijo delcev. Stopnje obrabe sesalne cevi, komore gonilnika, vodilnih lopatic in gonilnika naraščajo s koncentracijo delcev. Nasprotno pa se obraba v območju 1 na opornici z naraščajočo koncentracijo delcev najprej zmanjša, nato pa ponovno poveča. Poleg tega se z naraščajočo koncentracijo delcev povečujeta tlak na površinah ohišja in vodilnih lopatic ter turbulentna kinetična energija v sesalni cevi. Pri trifaznem toku trdnih delcev, tekočine in pare ob prisotnosti sedimentnih delcev se obraba med posameznimi sestavnimi deli turbine precej razlikuje. Ugotovljena je bila pozitivna korelacija med koncentracijo delcev in obrabo sesalne cevi, komore gonilnika ter vodilnih lopatic. V komori gonilnika je bila največja obraba gonilnika ugotovljena pri koncentraciji delcev 4,5 %. Kavitacija povečuje tlak na površinah vodilnih lopatic in sten ohišja, hkrati pa zmanjšuje turbulentno kinetično energijo v sesalni cevi in blaži erozijsko obrabo sten.*

Ključne besede *trifazni tok trdnih delcev, tekočine in pare, kavitacija ob prisotnosti sedimentnih delcev, cevna turbina, dvofazni tok trdnih delcev in tekočine, značilnosti obrabe*